# The effect of temperature and strain rate on the grain boundary sliding in a CM247 LC Ni-based superalloy processed with laser based powder bed fusion

Journal of Materials Research and Technology 28 (2024) 2466–2477

Contents lists available at ScienceDirect

Journal of Materials Research and Technology

journal homepage: www.elsevier.com/locate/jmrt

# The effect of temperature and strain rate on the grain boundary sliding in a CM247 LC Ni-based superalloy processed with laser based powder bed fusion

P.A. Martelli [a,b], I. Sabirov [c], M.A. Monclus [c], E. Bassini [a,b,d,*], G. Marchese [a,b], D. Ugues [a,b,d]

[a] Politecnico di Torino, Dip. Scienza Applicata e Tecnologia (DISAT), Italy
[b] Centro Interdipartimentale Integrated Additive Manufacturing IAM@PoliTO, Italy
[c] IMDEA Materials Institute, Getafe, 28906, Madrid, Spain
[d] Consorzio Nazionale della Scienza e Tecnologia dei Materiali (INSTM), Italy

ARTICLE INFO

Handling editor: L Murr

*Keywords:*
Nickel-based superalloys
Powder metallurgy
Heat treatment
Grain boundary sliding
Grain boundary
Plastic deformation mechanisms

ABSTRACT

The current work explores the meso-scale deformation behaviour of an additively manufactured CM247 LC at room and high temperatures. In particular, the study focuses on assessing grain boundary sliding (GBS), which can play a crucial role in the high-temperature deformation of superalloys. Specific samples were produced using the Laser Based Powder Bed Fusion technique (PBF-LB), heat treated and tested under monotonic compression in a Gleeble® system. Compression tests were carried out in a wide temperature range at two strain rates and the effect of testing parameters on GBS activity was studied. A thorough microstructural characterization of the PBF-LB material using EBSD and TEM revealed a $\gamma/\gamma'$ microstructure consisting of columnar grains decorated with Hf-rich MC carbides without any segregations of alloying elements. Qualitative and quantitative analysis of GBS was performed using FEG-SEM and AFM, and contribution of GBS into plastic deformation was estimated. It was demonstrated that GBS is activated at 760 °C. A direct correlation between the contribution of GBS into plastic deformation and testing temperature was found, while strain rate has the opposite effect. The highest GBS contribution (~32%) was recorded at 1093 °C/$10^{-3}$ $s^{-1}$. Finally, intergranular microcracking at triple junctions and along grain boundaries was observed when the material was tested at the highest temperatures (871 °C and 1093 °C). The effect of the temperature and the strain rate on the GBS activity in the PBF-LB material is discussed.

## 1. Introduction

Ni-based superalloys are widely used in the aeronautical and energy production fields due to their ability to preserve high mechanical strength at high temperatures and resistance to oxidation [1]. The exceptional mechanical properties are provided by both solid-solution [2] and precipitation strengthening mechanisms [3]. The achievement of these high-end performance is tightly bonded to the material microstructure and chemistry, in particular the quantity of Al and Ti are extremely relevant. At the same time, the increase of these elements, makes the material stronger and more stable at higher temperature, but weakens its formability and weldability, and introduces the risk of defects formation. Specifically, in the realm of aeronautics, stringent regulations govern the permissibility of material defects, and these guidelines are rigorously enforced on a daily basis in accordance with certification protocols outlined by manufacturers or governmental entities like the FAA (Federal Aviation Administration). While these regulations seamlessly apply to conventionally sourced materials, they are currently in a developmental phase for materials produced through Additive Manufacturing (AM). When it comes to AM components, the norm involves either aligning with existing certification protocols or searching through novel protocols specifically tailored for AM structural parts. The intricacy and seriousness of these protocols hinge on the criticality and failure mode of a component. These evolving protocols are designed to devise practical certification strategies that leverage the advantages of emerging AM technologies without compromising the safety of aircraft or space vehicle operations. They encompass a blend of in-depth insights into material properties, manufacturing processes, and

* Corresponding author. Politecnico di Torino, Dip. Scienza Applicata e Tecnologia (DISAT), Corso Duca Degli Abruzzi 24, 10129, Torino, Italy.
*E-mail address:* emilio.bassini@polito.it (E. Bassini).

https://doi.org/10.1016/j.jmrt.2023.12.131
Received 8 November 2023; Received in revised form 16 December 2023; Accepted 16 December 2023
Available online 21 December 2023

design considerations related to critical failure modes, potential defects, and part classification. Typically, these protocols offer guidance on optimal post-processing standards. For instance, recommendations may include the application of processes such as Hot Isostatic Pressing (HIP) to mitigate the criticality of internal defects impacting component functionality. Additionally, these protocols aim to enhance material microstructure and address anisotropy concerns. Remarkably, these protocols adhere to safe-life design methodologies that factor in the presence of internal crack-like defects. Through meticulous calculations of minimum critical flaw sizes, an allowable service life is defined, ensuring a comprehensive approach to structural integrity and safety in the realm of aeronautical engineering.

Among Ni-based superalloys, CM247 LC is characterised by a γ-FCC matrix reinforced by ordered $L1_2$ $Ni_3(Al,Ti)$ γ' precipitates [4,5]. Many studies have been conducted to assess the processability of this alloy using the Laser Based Powder Bed Fusion (PBF-LB) and its microstructural evolution during heat treatments due to the capability of additive manufacturing techniques to produce near-net shape (NNS) complex parts [4–7]. Ni-based superalloys are typically used in high-temperature environment, and it is important to assess their deformation behaviour in such conditions. Particularly, loading these materials at high homologous temperatures ($\geq 0.5T_m$) may trigger grain boundary sliding (GBS), when two grains slide with respect to each other along their boundary [8,9]. The grains then become incompatible with each other leading to failures with low ductility, unless the incompatibilities created by sliding are accommodated. Two main accommodation mechanisms are considered in the current literature. First, grain boundary diffusion, where vacancies flow along the grain boundaries, and the individual grains become elongated. This process is known as Lifshitz GBS. It typically occurs in fine grained materials deformed at very high temperatures [8]. Second, accommodation by dislocation glide and climb, where grains retain their original shape. The latter is referred to as Rachinger sliding, and it occurs in materials with larger grains [8]. In general, crystalline slip accommodates most of the plastic deformation in metals. Nevertheless, there are numerous reports where GBS accommodates a significant proportion of the total strain depending on the testing parameters [8]. High temperatures promote GBS due to enhanced diffusion coefficient and accelerated dislocation glide and climb. As it is well known, the self-diffusivity of an atom is correlated to the temperature by the Arrhenius-like relation given in (1):

$$D = D_0 e^{-\frac{Q}{RT}} \tag{1}$$

where $D_0$ is a pre-exponential term, Q is the activation energy for self-diffusion, R is the gas constant and T is the temperature [10]. Similarly, dislocation glide and climb processes are thermal-dependent [11], and dislocations' velocity (v) is correlated to T as given in (2) [10]:

$$v \propto e^{-\frac{Q}{RT}} \tag{2}$$

At the same time, it is recognised that low strain rates also promote GBS activity [12]. Atom diffusion and dislocation movements are necessary to relax the high stress concentration levels arising at the grain boundaries during the sliding due to strain incompatibilities [13]. If the local stresses are too high to be accommodated and the alloy faces a drop in ductility, inter-granular cracking can take place leading to failure [14]. For this reason, it is very important to assess the activity of GBS and its contribution to the plastic deformation of polycrystalline alloys which can be subjected to creep condition [15–17]. Simple monotonic uniaxial tests in a wide temperature and strain rate ranges have been widely used in literature for this purpose. Special attention was paid to this phenomenon occurring in ultrafine-grained Al alloys during their plastic deformation at relatively low temperatures [18]. Also, its key role in superplastic deformation of fine-grained Mg alloys was demonstrated [19]. There is a significant body of experimental research focusing on GBS and its quantification in light alloys [20–25]. On the contrary, very few experimental studies have been done to investigate the occurrence of GBS in Ni-based superalloys and its dependence on the microstructure and testing parameters. Torres et al. [26] focused on the GBS *in-situ* measurements on a Ni-based superalloy tested at high temperature. Takizawa et al. [27] analytically assessed the GBS as the controlling deformation mechanism in superplastic high-pressure sliding formability of Inconel 718 at high temperature. Others focus on molecular dynamics simulations rather than experimental studies [28,29]. AM is becoming increasingly important for producing complex shape parts for aeroengines [30].

However, the microstructures inherited from the AM are somewhat different than those obtained with traditional technologies, such as investment casting [30]. Alloys processed by AM typically show finer grains elongated along the building direction and crystallographic texture, which often depend on the process parameters and the scanning strategy [31–33]. These microstructures can significantly impact the final properties of the material, leading to mechanical anisotropy [34,35].

While there are several studies reporting the mechanical properties of additively manufactured Ni-based superalloy [36], their mesoscale deformation behaviour has not been investigated up to date. Understanding the mechanisms operating at high temperatures is crucial for microstructural design in these materials to achieve high performance at service temperatures. Particularly, GBS is a very important deformation mechanism controlling their high-temperature creep resistance. No works exploring the GBS activity in additively manufactured Ni-based superalloys can be found in the current literature. The main objective of the present work was to explore the GBS activity at different temperatures and strain rates in CM247 LC Ni-based superalloy processed by PBF-LB. Monotonic compression tests were performed to assess the influence of test temperature and strain rate on the deformation behaviour of the superalloy. The deformed samples were then analysed using Field-Emission Gun Scanning Electron Microscopy (FEG-SEM) and Atomic Force Microscopy (AFM) and a scheme was developed to analyse the contribution of GBS as a function of the testing parameters.

## 2. Materials and method

### 2.1. Material and samples production

The specimens were produced using a PrintSharp 250 PBF-LB system by Prima Additive equipped with a carbon steel building platform heated at 80 °C and a rubber recoater. Printing was performed under high purity Ar gas with an oxygen level lower than 0.1%. The parameters' ranges studied during the process optimization are reported in Table 1. Pre-alloyed gas atomized powder supplied by Praxair Inc. as NI-1230 was used as raw material. The chemical composition according to the manufacturer datasheet is reported in Table 2, while the volumetric powder size distribution measured through laser granulometry resulted in D10, D50 and D90 of 24.5 μm, 33.7 μm and 46.2 μm, respectively. Finally, apparent density and flowability were measured according to ASTM B212 and ASTM B213 and resulted in 4.63 ± 0.01 g $cm^{-3}$ and 12.9 ± 0.2 g $cm^{-3}$, respectively.

The powders were subjected to further chemical analysis to assess the average content of the main interstitial elements: C and S were determined via NIR oxygen combustion using a Leco CS 744. At the same time, O, N and H were evaluated via inert gas fusion in a Leco ONH 836 machine. Results are shown in Table 3.

Ten specimens for compression tests were produced in a single job as cylinders having a height of 17 mm (aligned along the building

**Table 1**
Parameters range.

| Laser power [W] | Scan speed [mm $s^{-1}$] | Hatching distance [mm] | Stripes-head overlapping |
|---|---|---|---|
| 170–195 | 1000–1900 | 0.03–0.08 | 0.1–0.2 |

**Table 2**
Chemical composition (wt.%) of CM247LC alloy according to producer's technical datasheet.

| Ni [%] | Cr [%] | Co [%] | W [%] | Ta [%] | Mo [%] | Al [%] | Ti [%] | Hf [%] | Zr [%] |
|---|---|---|---|---|---|---|---|---|---|
| Bal. | 8.0 | 9.3 | 9.7 | 3.6 | 0.5 | 5.2 | 0.8 | 1.7 | 0.01 |

**Table 3**
Residual elements (wt.%) in the raw powder.

| C [%] | S [ppm] | O [%] | N [%] | H [ppm] |
|---|---|---|---|---|
| 0.083 (±0.001) | 4.79 (±0.08) | 0.014 (±0.002) | 0.0036 (±0.0002) | 7.89 (±1.38) |

direction) and a diameter of 10 mm (Fig. 1). A flat surface of 3.5 mm of width was also added to the model to measure the GBS after compression tests through SEM and AFM. From now on this surface will be referred to as "flat surface". The wires of a K-type thermocouple were welded on the midsection of each tested sample to control the temperature with the accuracy of ±1 °C (Fig. 1). The welding was performed according to standard procedures applied in Gleeble testing. It should be noted that the heat-affected zone in the subsurface area is negligibly small compared to the sample size. It has been well established that it does not affect the mechanical properties of samples tested in Gleeble, and this welding procedure has been employed in laboratories worldwide [37, 38].

### 2.2. Sample post processing and heat treatment

The manufactured samples were cut from the building platform via Wire Electro-Discharge Machining (WEDM), manually sandblasted and stress relieved at 1080 °C for 2 h in an air furnace. Then, the samples underwent Hot Isostatic Pressing (HIP) in a Quintus QIH 15L machine equipped with a Molybdenum furnace to reduce the internal flaws population. This step was performed below the γ' solvus temperature. Pressure and temperature were increased simultaneously, and the samples were cooled to room temperature at a rate of 15 °C $min^{-1}$ (calculated from HIP temperature to 400 °C) after soaking for 3 h.

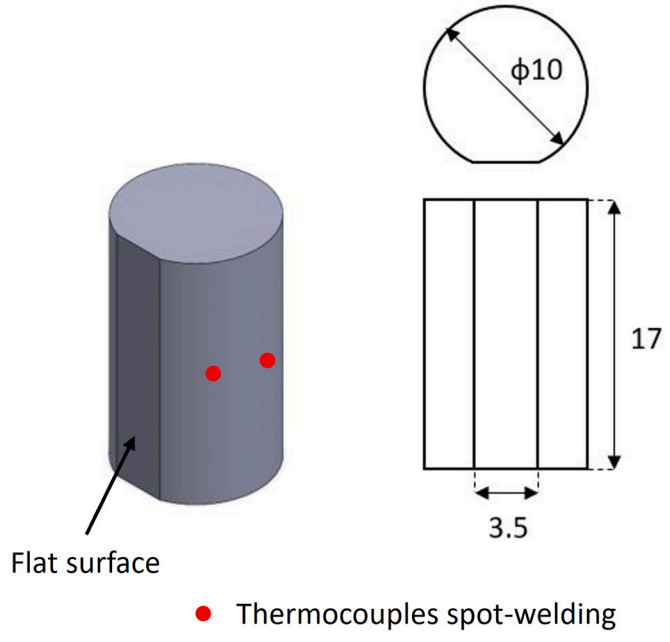


**Fig. 1.** Raw specimen produced for the compression tests (dimensions in mm).

Subsequent heat treatment was optimized elsewhere by the authors [4]. The recipe is reported briefly:

- Solution annealing (SA): 1245 °C for 2 h + fast cooling at 100 °C $min^{-1}$;
- I aging: 1080 °C for 4 h + fast cooling at 50 °C $min^{-1}$;
- II aging: 870 °C for 6 h to stabilize the microstructure and promote a further precipitation of fine γ'.

The whole cycle was applied in a low-pressure furnace TAV minijet. Even if other literature works use 1260 °C as a SA temperature, authors pursued the lower temperature to avoid the formation of thermally induced porosities (TIPs) [4]. Furthermore, performing the SA at a lower temperature could be of industrial interest since it reduces the related costs and increases the available number of certified equipment and subcontractors in the market.

### 2.3. Machining and polishing

All specimens were machined to a final length of 15 mm to ensure that the two circular faces were parallel. Furthermore, the flat surface was ground with SiC sandpapers up to 1200 grid and polished with 6-3-1 μm diamond suspensions. Finally, 0.04 μm colloidal silica suspension was used to obtain the mirror-like surface. Ethanol and ultrasonic baths were used to remove any debris resulting from the polishing steps.

### 2.4. Compression test using the Gleeble® system

Compression tests were performed using a Gleeble® 3800 system under constant strain rates of $10^{-3}$ $s^{-1}$ and $10^{-4}$ $s^{-1}$ at room temperature (RT), 649 °C, 760 °C and 871 °C, while only the strain rate of $10^{-3}$ $s^{-1}$ was used during the exposure at 1093 °C due to creep of anvils detected during testing at low strain rate of $10^{-4}$ $s^{-1}$. Prior to the tests, the height of each sample was measured to calculate the final deformation. Based on the authors' previous experience [18], a total plastic strain of ~8% was set as a target for the GBS to be easily detectable. This value ensured that GBS events could be observed leaving the surface flat enough for the following analysis using AFM. Samples were heated via Joule effect with a constant heating rate of 10 °C $s^{-1}$, and temperature was controlled using a K-type thermocouple as mentioned above (Fig. 1).

### 2.5. Microstructural assessment

The microstructure of the as-treated alloy was thoroughly studied before compression testing. The Electron Backscatter Diffraction (EBSD) analysis was performed using an Oxford Symmetry detector mounted on a focused ion beam-scanning electron microscope FIB-SEM TESCAN S9000G by Tescan. The specimens' tilting was kept at 70°, with a voltage of 20 kV and rolling direction parallel to the building axis of the sample. The microstructure at grain boundaries was evaluated using a Zeiss EVO15 SEM and a FEG S/TEM (Talos F200X, FEI) operated at an accelerating voltage of 200 kV. Elemental mapping was carried out using energy dispersive spectroscopy (EDS) SuperX detector from FEI & Bruker. The foils for TEM observations were cut from a heat-treated sample and prepared with a TenuPol 5 (Struers®) by twin-jet electro-polishing with a solution consisting of 10% perchloric acid ($HClO_4$), 30% butanol and 60% ethanol at −25 °C under an operating voltage of 20 V.

### 2.6. Grain boundary sliding quantification

After being tested, the specimens were subjected to further inspections to assess the deformation mechanisms and evaluate the activity of GBS. For practical reasons, the authors chose the out-of-plane measurement among the possible quantification methods, which is shown in Fig. 2.

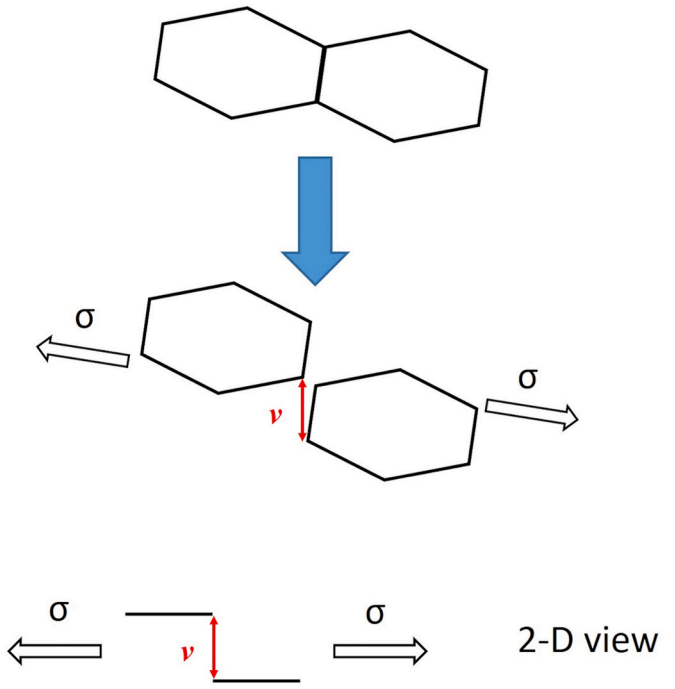


**Fig. 2.** GBS representation and out-of-plane offset component.

The corresponding equation used for the evaluations was reported in the work of Langdon [9] for polished surfaces (3):

$$\varepsilon_{gbs} = 1,1 \bullet \frac{\overline{v}_r}{\overline{l}_r} \tag{3}$$

where $\varepsilon_{gbs}$ is the plastic deformation related to the grain boundary sliding, $\overline{v_r}$ is the displacement between grains perpendicular to the polished surface and $\overline{l}_r$ the mean distance between sliding events randomly measured. Using Equation (4), it is possible to calculate the GBS relative contribution ($\xi$) to the total plastic deformation ($\varepsilon_{p,tot}$) as a value ranging from 0 to 1 [9]:

$$\xi = \frac{\varepsilon_{gbs}}{\varepsilon_{p,tot}} \tag{4}$$

There are no standard measurement rules for the GBS quantification, so a scheme was defined by the authors. The surface relief of the deformed specimens was analysed using a FEG-SEM APREO 2S LoVac to assess the activity of GBS during plastic deformation. The distance between sliding events was recorded by drawing six lines (three parallels and three perpendiculars to the load direction) on five SEM images randomly taken at a magnification of 500x, as represented by the red lines in Fig. 3. For each line, the number of GBS events was counted and divided by the length of the line. The mean value of the six different counts was used to quantify $\overline{l}_r$. Once the SEM observation was completed, the specimens were analysed with a Park XE150 Atomic Force Microscope (AFM) to measure nine out-of-plane offsets; their mean value was used to quantify $\overline{v}_r$. The area subjected to both FEG-SEM and AFM analyses was in the midsection of the specimen's flat surface (Fig. 3).

## 3. Results and discussion

### 3.1. Microstructural assessment

Fig. 4a shows the microstructure of the as-treated material, while Fig. 4b presents an EBSD map of the same sample. Annealing the samples at 1245 °C led only to a partial dissolution of γ' and grains structure recovery from PBF-LB process. Fig. 4 confirms that annealing the PBF-LB

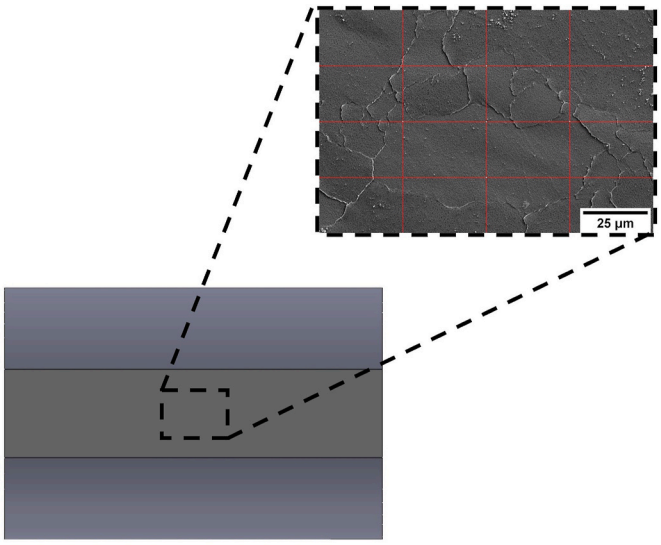


**Fig. 3.** Investigated area after compression tests with detail on the lines drawn for $\overline{l}_r$ quantification.

CM247 LC at 1245 °C may not be effective in achieving complete recovery of the PBF-LB structure and γ' dissolution primarily due to uncertainties associated with the industrial furnaces. Fig. 4a shows the coexistence of small and cubic γ' precipitates (marked by the green arrow) as well as large and irregular ones (indicated by the red arrow), which were retained from the HIP process [4,39]. The larger γ' precipitates are primarily found at the grain boundaries. Also, SEM images reveal that the grain boundaries appear to be decorated with Hf-rich MC carbides (indicated by the blue arrow) [4,40].

Fig. 4b displays relatively large grains (~60 μm) that are predominantly elongated along the building direction. The aspect ratio (AR) of the grains, determined as the ratio between the major and the minor axes of the fitting ellipse obtained from EBSD characterisation, is reported as 3.5 ± 2.1. The grain morphology is noteworthy because some previous publications reported that elongated grains have a reduced propensity for sliding compared to the equiaxed ones [41].

The majority of grain boundaries observed in Fig. 4 are non-serrated. This can be attributed to the relatively rapid cooling rate (100°C/min) employed after SA heat treatment (see Section 2.2) which results in non-serrated grain boundaries in Ni-based superalloys [39]. Furthermore, the SA treatment performed at 1245 °C left a significant fraction of Low-Angle Grain Boundaries (LAGB <10°), estimated to be approximately 32%.

Primary γ′ precipitates are usually intergranular and only form when the superalloy is heat treated below the γ-solvus temperature. Annealing above the γ'-solvus dissolves the primary γ′ and subsequent solution cooling, at rates of ≲10 °C/min results in the formation of intragranular secondary γ′ precipitates during the early stage of cooling. Further cooling results in the growth of secondary γ′ precipitates until the low elemental diffusivities of the γ stabilizing elements make it difficult for these elements to reach the comparatively coarse secondary γ′. This leads to supersaturation of these elements within the γ matrix and consequently drives the nucleation of additional nanosized intragranular tertiary γ′ [42,43].

FEG S/TEM analysis was conducted to assess the potential presence of segregations at grain boundaries, which could influence the GBS process in polycrystalline alloys [44,45]. Fig. 5a shows an overall view of a grain boundary (indicated by the white arrow) separating two regions rich in the γ matrix. It is noteworthy that no chemical segregations were observed, indicating that the SA treatment effectively eliminated any chemical inhomogeneity present in the matrix resulting from the PBF-LB process. Additionally, Fig. 5a displays the previously mentioned

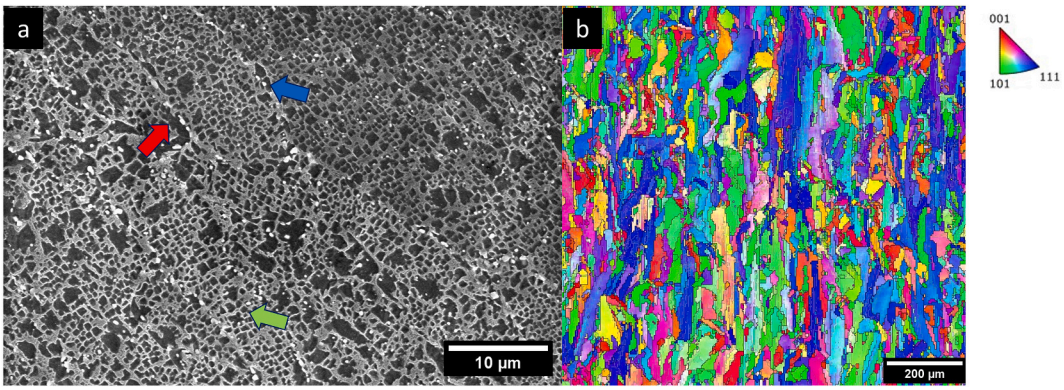


**Fig. 4.** Microstructure after heat treatment: a) general microstructure observed with SEM and b) EBSD IPF map.

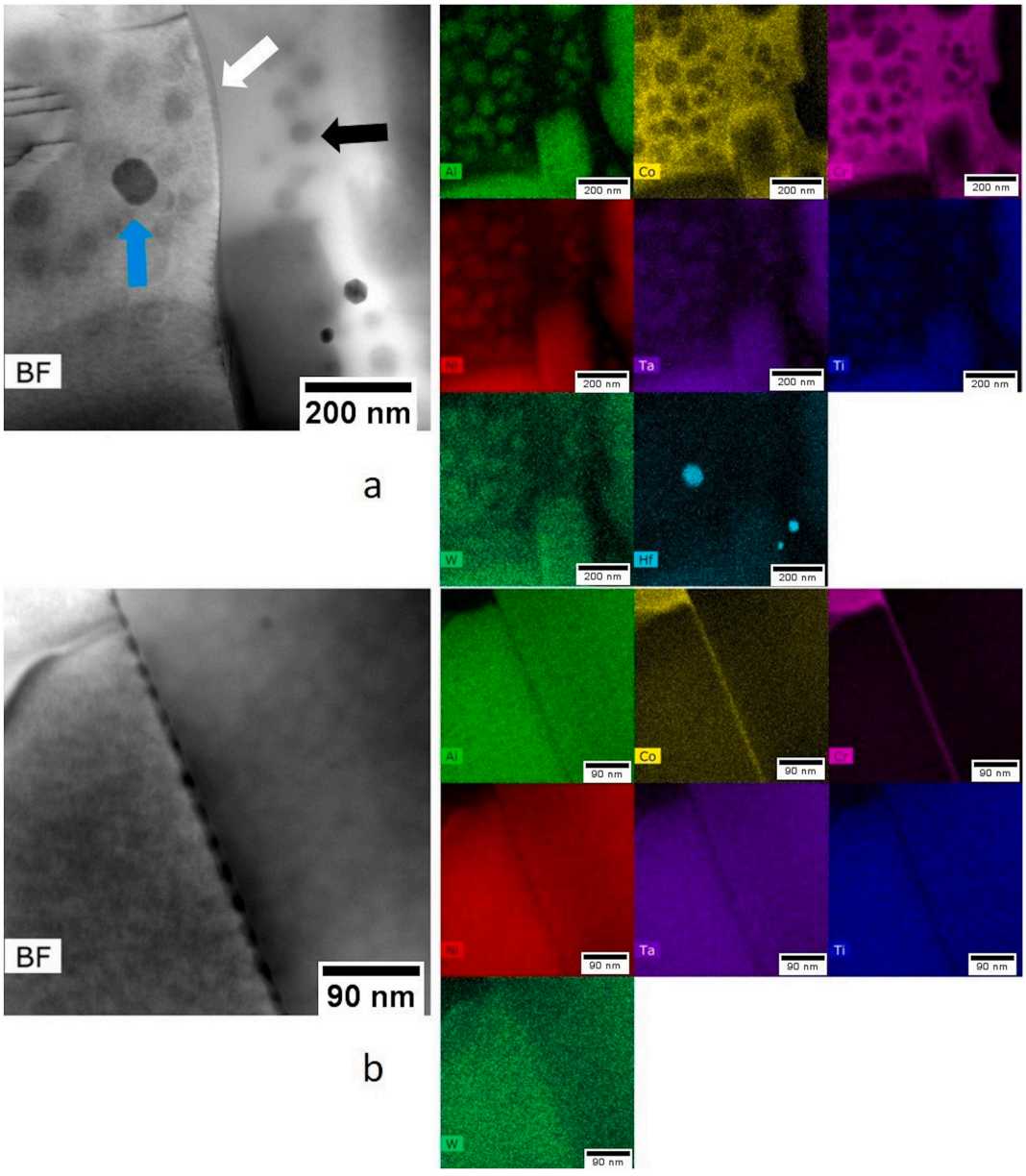


**Fig. 5.** EDS mapping performed at the grain boundary: a) general view and b) focus on γ-γ' border. Al is represented by light green, Co by yellow, Cr by light purple, Ni by red, Ta by dark purple, Ti by dark blue, W by dark green and Hf by light blue.

Hf-rich MC carbides (indicated by light-blue arrow).

However, they are not precisely located on the boundary itself but are several hundreds of nanometres away from it. Very thin (<100 nm) tertiary γ' precipitates can be observed within the γ-channels (indicated by the black arrow). In Fig. 5b, an EDS map was performed at a very high magnification to highlight a grain boundary that separates two γ' particles. Even in this case, the grain boundary exhibits a chemical composition similar to that of the γ phase. Consequently, even when two γ' particles are divided by a grain boundary, dislocations can find a preferential path along which they can slide, partially bypassing the resistance imposed by the γ-γ' interface.

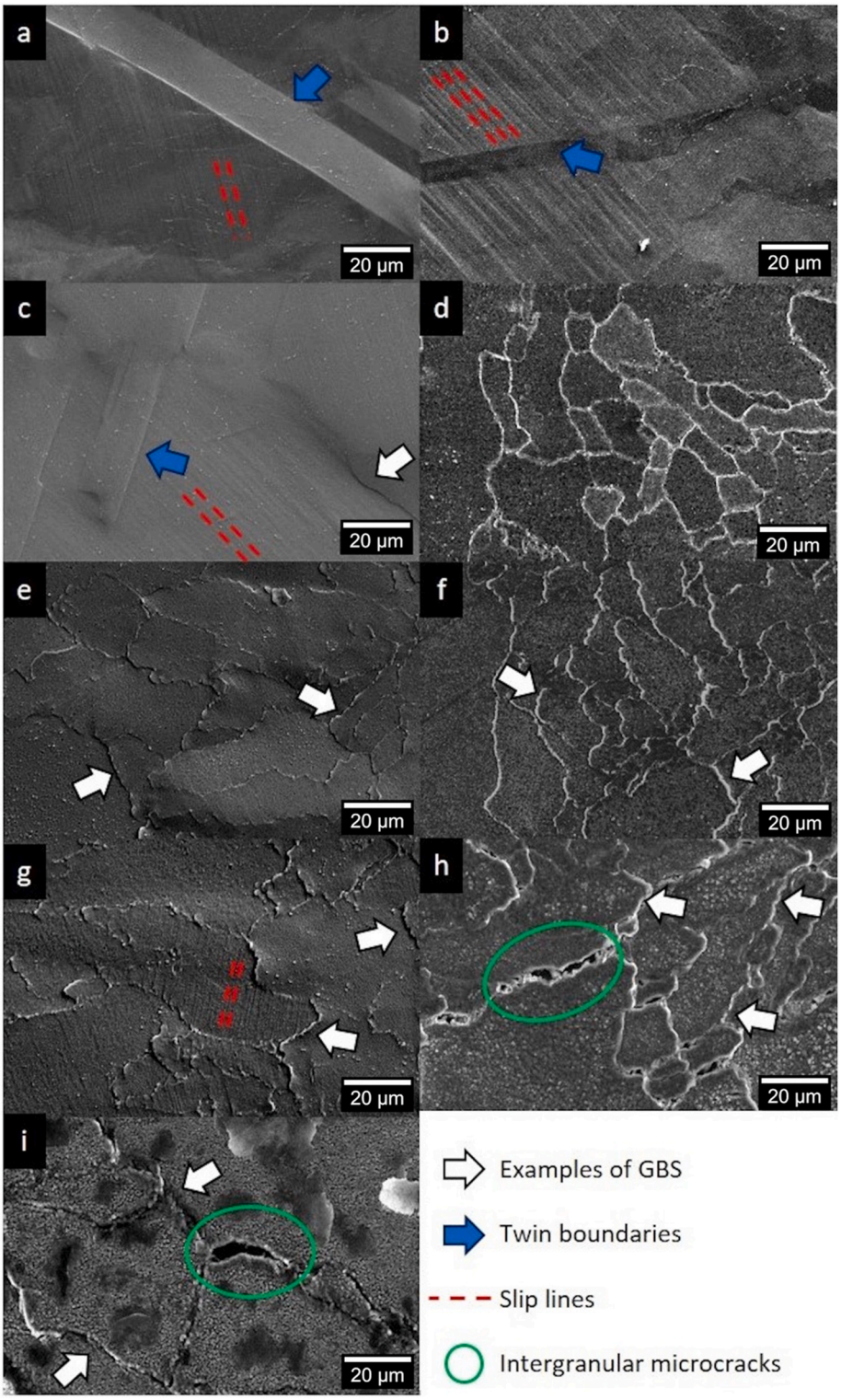


**Fig. 6.** Morphological characterization of samples' surfaces. On the left, samples tested with a strain rate of $10^{-3}$ $s^{-1}$ at a) RT, c) 649 °C, e) 760 °C, g) 871 °C and i) 1093 °C. On the right, samples tested with a strain rate of $10^{-4}$ $s^{-1}$ at b) RT, d) 649 °C, f) 760 °C and h) 871 °C.

### 3.2. SEM assessment of samples tested at different temperatures and strain rates

In order to evaluate the influence of temperature and strain rate on GBS activity, the surface relief of the tested specimens was examined using FEG-SEM. To illustrate the qualitative evolution of surface morphology, a comprehensive synoptic table is presented in Fig. 6. It provides an overview of the observed changes in surface topography under different temperature and strain rate conditions, allowing for a qualitative assessment of the GBS behaviour.

Fig. 6a and b illustrate the surface relief after compression testing at RT with different strain rates. No GBS is observed at RT for both applied strain rates, but intense slip activity is detected (marked by red lines). Twin boundaries are also clearly visible on the surface (marked by blue arrows). Fig. 6c and d present SEM images of the surface relief after testing at 649 °C with strain rates of $10^{-3}$ and $10^{-4}$ $s^{-1}$, respectively. The sample tested at 649 °C/$10^{-3}$ $s^{-1}$ exhibits well-pronounced slip lines (marked by red lines), while only sporadic sliding events are recorded, as marked by the white arrow in Fig. 6c. In the latter specimen, straight highly deformed boundaries can be observed, which are identified as twins (marked by blue arrows). No significant GBS is noticeable after testing at 649 °C/$10^{-4}$ $s^{-1}$ (Fig. 6d). These observations confirm that GBS is practically inactive up to 649 °C.

Fig. 6e and f show the surface relief of specimens tested at 760 °C. GBS is now activated throughout the surface (indicated by white arrows). Fig. 6g and h illustrate the surfaces after testing at 871 °C with strain rates of $10^{-3}$ and $10^{-4}$ $s^{-1}$, respectively. GBS events (marked by white arrows) are observed after the test performed at 871 °C/$10^{-3}$ $s^{-1}$ (Fig. 6g), as expected. Slip lines (marked by dashed red lines) are still recognizable within some grains despite a slight surface oxidation. The sample subjected to the 871 °C/$10^{-4}$ $s^{-1}$ test exhibits more pronounced GBS activity (Fig. 6h). Additionally, some microcracks are formed along grain boundaries (marked by green circles) and at triple junctions. Finally, Fig. 6i shows the surface relief after the test conducted at 1093 °C/$10^{-3}$ $s^{-1}$. Intense GBS (marked by white arrows) and intergranular microcracking (indicated by green circles) can be observed.

### 3.3. Qualitative AFM analysis of surface relief

The outcomes of AFM analysis are consistent with the observations made using SEM (Section 3.2). The AFM 3D map of the deformed surface clearly indicates that the primary mechanism of plastic deformation at RT is dislocation glide (Fig. 7). Dislocations were observed to traverse twin boundaries, as evidenced by the AFM scan. The mechanism of dislocation transmission through twin boundaries in Ni-base superalloys has been previously proposed by different authors [46,47]. The gliding dislocations slip through a twin boundary when the slip plane with the highest Taylor factor intersects the twin boundary. Furthermore, recent studies [48] have documented strain localization at twin boundaries, which is believed to result in the appearance of twins on surfaces of

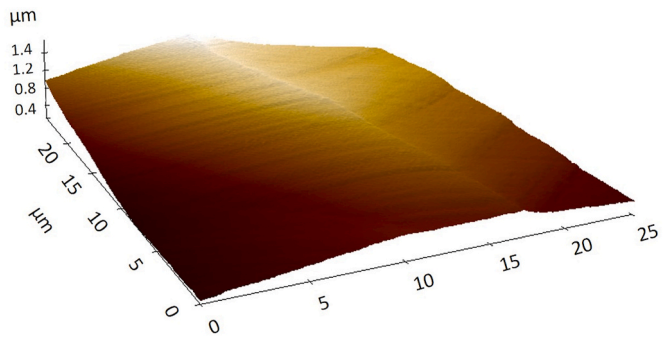


**Fig. 7.** Transmission of slip lines through twin boundaries under AFM observed in the sample RT/$10^{-3}$ $s^{-1}$.

specimens deformed at RT. The absence of GBS events makes this mechanism particularly visible.

Sporadic GBS events were observed on the surface of specimens tested at 649 °C. Fig. 8a presents an example of such an event, where two distinct grain boundaries underwent sliding during deformation with a strain rate of $10^{-3}$ $s^{-1}$ (marked by red circle). However, these events were confined to a limited spatial extent, spanning only a few microns. Additionally, under AFM, only rare occurrences similar to the one reported have been recorded for both the specimens tested at 649 °C. In the case of the specimen tested at 649 °C/$10^{-4}$ $s^{-1}$, the presence of γ' particles being cut by dislocation glide was evident (Fig. 8b). This behaviour aligns with the observations made by Stinville et al. [46].

Fig. 9 illustrates a surface reconstruction obtained through AFM for the specimens tested at 760 °C. In both cases, the occurrence of GBS (red circle in Fig. 9a) involves a greater number of grains compared to the specimens tested at 649 °C. However, the intensity of these events remains relatively low and comparable to what was observed at 649 °C. Fig. 9a and b indicate that the intensity of the GBS is consistent across different grains and is evenly distributed throughout the examined area. Nonetheless, it is important to note that GBS does not affect all grains, as some of them exhibit no evidence of sliding.

Surface reconstructions for specimens tested at 871 °C with strain rates of $10^{-3}$ $s^{-1}$ and $10^{-4}$ $s^{-1}$ are presented in Fig. 10a and b, respectively. In these cases, the occurrence of GBS is more pronounced, and its intensity is significantly enhanced by the lower strain rate. To emphasize the intensity of GBS activity, a line scan is shown in Fig. 10c. In this plot, the Y-axis represents the relative position of the AFM tip with its 0-position set at the beginning of the analysis. The X-axis corresponds to the length of the line scan.

Finally, Fig. 11 depicts the surface reconstruction obtained through AFM following the test conducted at 1093 °C with a strain rate of $10^{-3}$ $s^{-1}$. The figure reveals the formation of prominent large steps, which are a consequence of intense sliding events occurring at this high temperature. The intergranular microcracking is considerably more pronounced at this high temperature. Additionally, Fig. 11b provides an example of a line scan that highlights the activity of GBS.

Based on the previous findings, it is indicated that once the GBS is activated, it triggers the reciprocal sliding of adjacent grains according to the scheme illustrated in Fig. 12. The displacement resulting from this sliding can be described by the sliding vector $\vec{S}$, which is made of the three components *v, u* and *w*.

In the current literature it has been well established that the relative displacement of the grains results in strain incompatibilities at the grain boundaries, which lead to the stress concentration at the multiple junction points due to dislocations pile ups (as indicated by the white arrow in Fig. 13a) [13]. At very high testing temperatures, the stress concentration at these junctions accompanied by insufficient accommodation leads to the nucleation of voids (or cavities). These voids act as stress concentrators, promoting the formation and propagation of intergranular microcracks (as shown in Fig. 13b). The stress/strain ahead of the crack leads to further cavity nucleation and growth by interlinking with new cavities formed ahead of crack tip, as one can see on Fig. 6h [49]. The formation of cavities at the multiple junctions can be visually represented as illustrated in the schematic of Fig. 13c, where one of these cavities is formed due to the reciprocal displacement of the neighbouring grains. It should be noted that no particle free zones (PFZ) are observed in the vicinity of grain boundaries of all tested samples, thus pointing at dislocation glide as the main accommodation mechanism of the GBS process independently on the testing parameters [8]. Therefore, it can be concluded that the Rachinger sliding takes place during plastic deformation of the studied material.

### 3.4. Grain boundary sliding quantification

After examining the morphological characteristics of the deformed

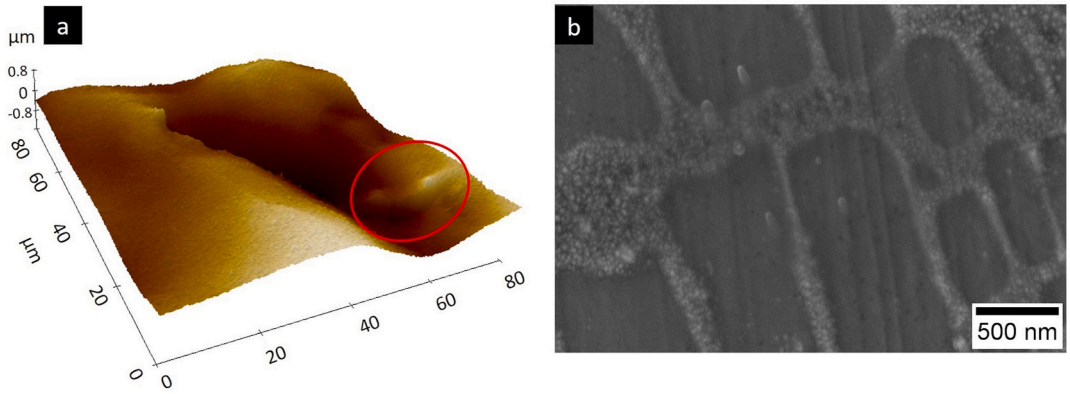


**Fig. 8.** a) Surface 3D reconstruction under AFM for the specimen tested at 649 °C with strain rate of $10^{-3}$ $s^{-1}$ (red circle indicates GBS) and b) detail on the γ' particles cut by dislocation activity

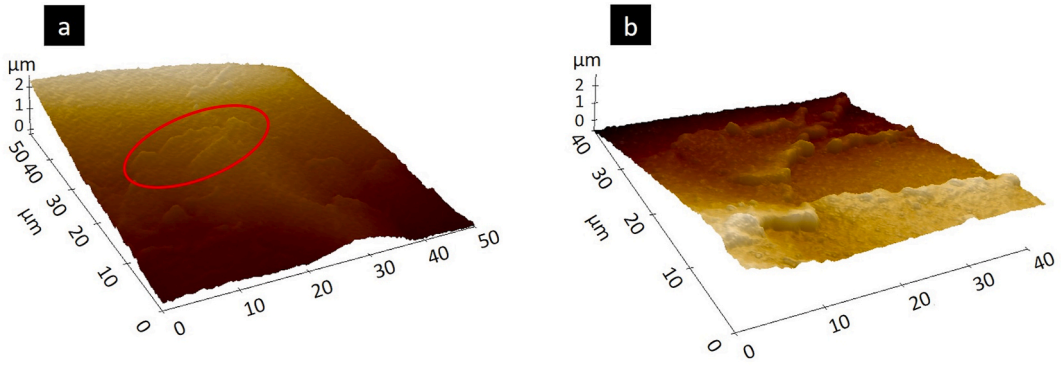


**Fig. 9.** Surface 3D reconstruction under AFM for the specimens tested at 760 °C with strain rate of a) $10^{-3}$ $s^{-1}$ and b) $10^{-4}$ $s^{-1}$..

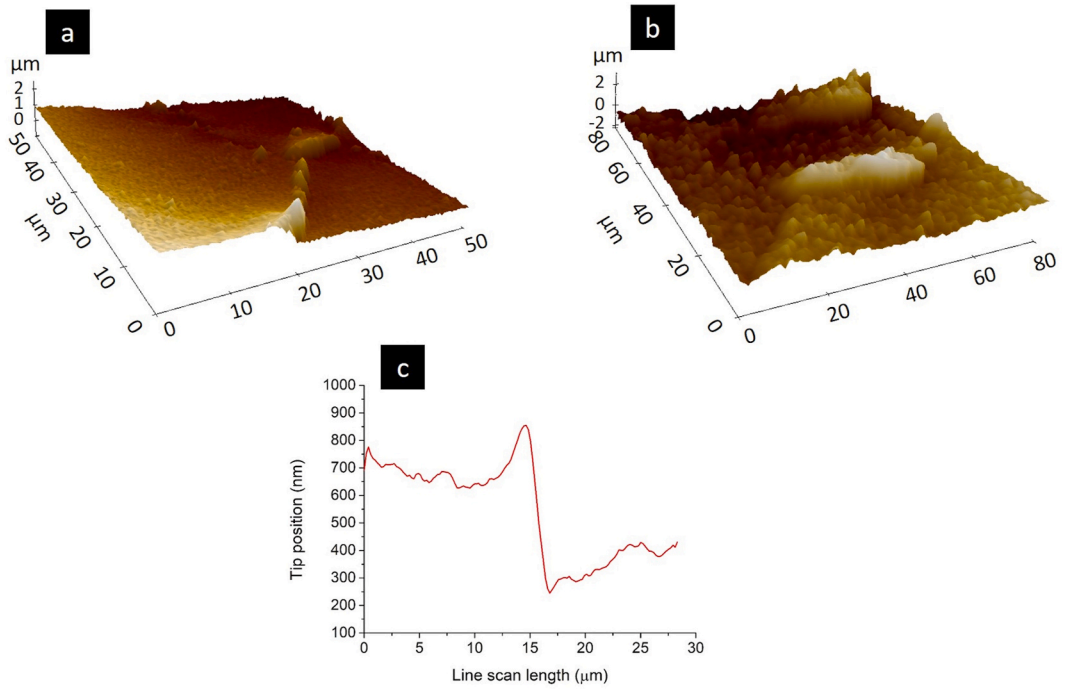


**Fig. 10.** Surface 3D reconstruction under AFM for the specimens tested at 871 °C with strain rate of a) $10^{-3}$ $s^{-1}$ and b) $10^{-4}$ $s^{-1}$ and c) example of a line scan performed across a GBS event.

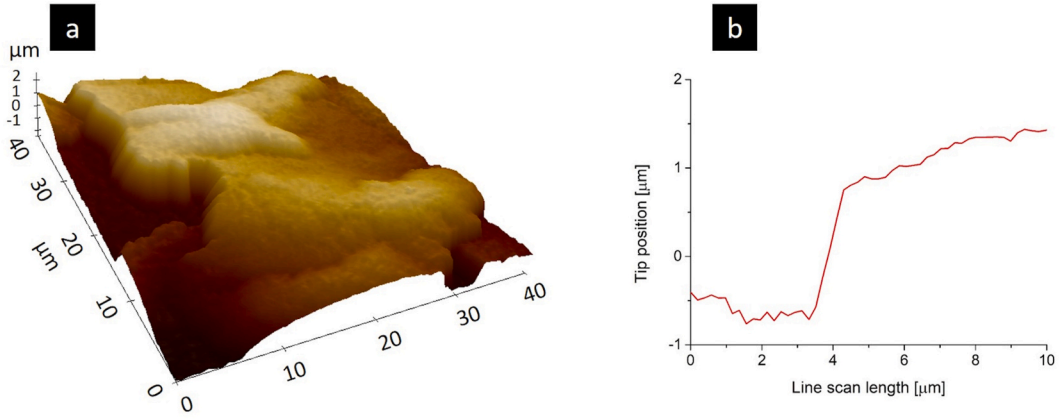


**Fig. 11.** Surface 3D reconstruction under AFM for the specimens tested at 1093 °C with strain rate of $10^{-3}$ $s^{-1}$ and b) example of a line scan performed across a GBS event.

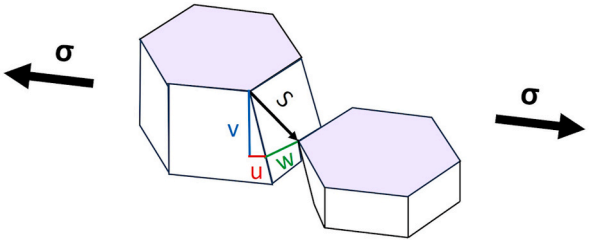


**Fig. 12.** Sliding mechanism of neighbouring grains.

specimens, the quantitative analysis of GBS contribution (ξ) to the overall plastic deformation of PBF-LB CM247 LC alloy was conducted. The measurement process involved determining the out-of-plane offsets ($v_r$) and mean distances between GBS events ($l_r$). The AFM 3D maps and images captured using FEG-SEM were utilized for this purpose. The measured values of these parameters for various test conditions are presented in Table 4.

The out-of-plane offsets remain constant at 649 °C at both strain rates ($10^{-3}$ $s^{-1}$ and $10^{-4}$ $s^{-1}$), indicating that the intensity of sliding events is not influenced by the strain rate at this temperature. Due to the rarity of GBS at 649 °C, an actual distance between sliding events could not be determined. To account for this, the authors chose to set a value of 1 mm, which is a realistic approximation based on surface observations. At 760 °C/$10^{-3}$ $s^{-1}$, there is a slight increase in the out-of-plane offsets compared to the specimens tested at 649 °C. In this case, the mean distance of GBS events was measurable and found to be 70 μm. The main difference between the tests performed at 760 °C at $10^{-3}$ $s^{-1}$ and at $10^{-4}$ $s^{-1}$ is the sliding intensity. The average out-of-plane offsets are 313 nm and 597 nm, respectively. However, the distance between these events does not show significant variation. Despite undergoing plastic

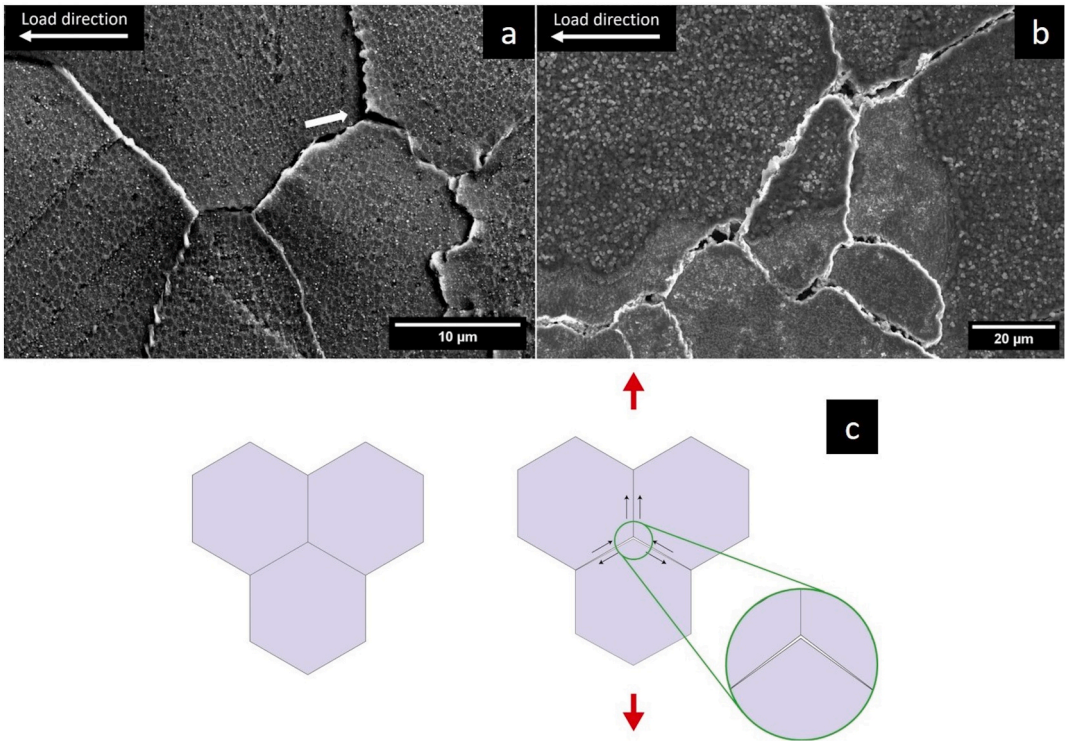


**Fig. 13.** Effect of the strain incompatibilities at the multiple junction points: a) concentration of GBS at the lower temperatures (760 °C/$10^{-3}$ $s^{-1}$), b) inter-granular microcracks formation at the higher temperatures (871 °C/$10^{-3}$ $s^{-1}$) and c) visual description of cavities formation.

**Table 4**
Out-of-plane offsets intensity ($v_r$) and mean distance ($l_r$) calculated for all the samples.

| Temperature [°C] | Strain rate [$s^{-1}$] | $v_r$ [nm] | $l_r$ [μm] |
|---|---|---|---|
| 649 | $10^{-3}$ | 251 ± 156 | 1000[a] |
| 760 | $10^{-3}$ | 313 ± 127 | 70 ± 22 |
| 871 | $10^{-3}$ | 552 ± 225 | 46 ± 7 |
| 1093 | $10^{-3}$ | 1459 ± 697 | 57 ± 10 |
| 649 | $10^{-4}$ | 257 ± 56 | 1000[a] |
| 760 | $10^{-4}$ | 597 ± 93 | 77 ± 10 |
| 871 | $10^{-4}$ | 1976 ± 942 | 106 ± 33 |

[a] Values approximated due to the very rare appearance of sliding events.

deformation for a longer duration, there is no notable increase in the number of activated grain boundaries. The concept of "activated" boundaries was discussed in Ref. [50]. This observation in the studied materials could be attributed to the morphology of grain boundaries. Experimental evidence suggests that serrated grain boundaries in Ni-based superalloys are effectively locked for sliding during plastic deformation, while non-serrated grain boundaries undergo sliding [51]. From the SEM images taken at higher magnifications (Fig. 13a and b), it is evident that the grain boundaries showing sliding are non-serrated. As the test temperature increases to 871 °C at a strain rate of $10^{-3}$ $s^{-1}$, both the intensity and the mean distance of the sliding events increase, indicating that more grain boundaries are able to slide. The GBS intensity at 871 °C/$10^{-4}$ $s^{-1}$ shows a significant increase ($v_r > 1000$ nm), while the spacing between events tends to be higher indicating a lower frequency. This behaviour may be attributed to inter-granular microcracking, which could result in local stress relaxation. A similar trend can be observed at 1093 °C/$10^{-3}$ $s^{-1}$ in terms of intensity, although the mean distance of the sliding events is lower.

Finally, the value of ξ representing the GBS contribution into plastic deformation, was calculated using Equations (3) and (4) and plotted in Fig. 14 as a function of temperature and strain rate. The calculated ξ values are normalized, ranging between 0 and 1, where 0 represents the absence of GBS and 1 represents the exclusive occurrence of GBS without any other plastic deformation, which is not realistic. At 649 °C, the estimated GBS contribution is less than 1% based on the given reference value of 1 mm for the mean distance between GBS events. This indicates that the plastic deformation is provided predominantly by dislocation gliding, whereas contribution of GBS is negligibly small, and the contribution of diffusion is also very low due to low homologue temperature. For the 1093 °C test, some steps were higher than the measurement range in AFM (±4 μm), suggesting that the actual GBS contribution would be higher. It can be concluded that the GBS contribution at 1093 °C is at least 32% of the total plastic deformation. In the specimen tested at 760 °C with a strain rate of $10^{-3}$ $s^{-1}$, the GBS contribution was calculated to be 0.062 (6.2%), and at a strain rate of $10^{-4}$ $s^{-1}$ it was 0.089 (8.9%). The GBS contribution increases further to 0.134 (13.4%) and 0.245 (24.5%) at 871 °C. It is evident that ξ increases with the rise in testing temperature and the decrease in strain rate. This behaviour is consistent with the influence that these test parameters have on both atomic diffusion and dislocation mobility, affecting the occurrence and intensity of GBS.

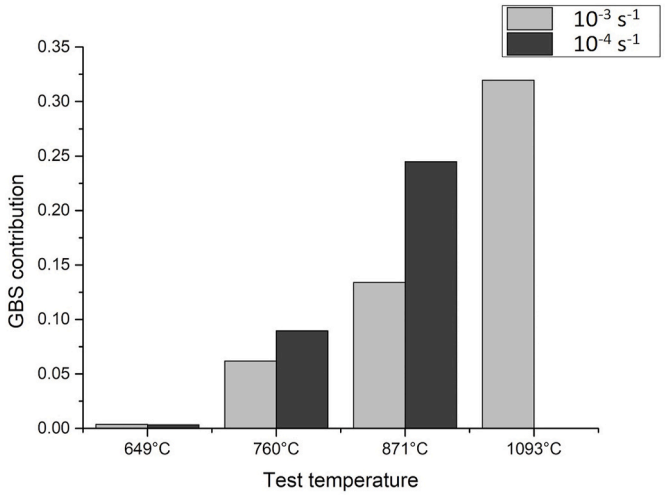


**Fig. 14.** GBS contribution (ξ) as a function of test temperature and strain rate.

## 4. Conclusions

Monotonic compression tests in a wide temperature range and two different strain rates were performed on CM247 LC samples processed with PBF-LB. SEM and AFM analyses of the surface relief of tested samples were performed, and the GBS activity was analysed as a function of temperature and strain rate. Contribution of GBS into total plastic deformation was estimated. The following conclusions can be drawn:

- The contribution of GBS (ξ) to the total plastic deformation was estimated by measuring the out-of-plane offsets using AFM. It was found that ξ value increases with increasing temperature (T) and decreasing strain rate ($\dot{\varepsilon}$). This observation is consistent with the enhancing effects of T and $\dot{\varepsilon}$ on grain boundary diffusional processes and dislocation mobility.
- Despite the elongated and non-equiaxed grain structure (aspect ratio AR = 3.5 ± 2.1), GBS significantly contributes to the plastic deformation at temperatures of 760 °C and above.
- Microstructural observations revealed the absence of chemical segregations at grain boundaries which could promote GBS activity. Additionally, large matrix γ channels between precipitated γ' particles were observed, potentially facilitating diffusion processes and dislocation mobility involved in GBS. Absence of PFZ in the vicinity of grain boundaries of the tested samples indicates that the Rachinger sliding takes place and GBS process is accommodated mainly by dislocation glide at all studied temperatures and strain rates.
- Intergranular microcracking starting at triple junctions was observed at 871 °C/$10^{-4}$ $s^{-1}$ and 1093 °C/$10^{-3}$ $s^{-1}$, indicating the intense stress concentration caused by GBS at triple junctions.

Given the intense intergranular microcracking observed at 871 °C and 1093 °C, it is recommended to avoid or minimize the occurrence of GBS in CM247 LC alloy under in-service creep conditions in order to enhance its mechanical properties at high temperatures. To achieve this, future studies will focus on raising the SA temperature treatment. By increasing the SA temperature, complete γ' solution and recovery of the PBF-LB structure can be achieved. This approach aims to modify the material's microstructure and eliminate or reduce the presence of grain boundaries that are susceptible to GBS, thereby improving the alloy's resistance to intergranular microcracking and enhancing its overall mechanical performance at elevated temperatures.

## Authorship contribution statement

**Pietro Antonio Martelli**: conceptualization, writing, editing, samples production, experimental investigation and data analysis. **Ilchat Sabirov**: supervision, conceptualization, experimental investigation, data analysis and editing. **Miguel Alberto Monclus**: experimental investigation, data analysis. **Emilio Bassini**: heat treatments, conceptualization and editing. **Giulio Marchese**: experimental investigation. **Daniele Ugues**: supervision and conceptualization.

## Data availability

All the experimental data to reproduce these findings are already

contained in the paper and further material can be disclosed contacting the corresponding author.

## Declaration of competing interest

The authors declare that they have no known competing financial interests or personal relationships that could have appeared to influence the work reported in this paper.

## Acknowledgements

This project has received funding from the Clean Sky 2 Joint Undertaking under the European Union's Horizon 2020 Research and Innovation Programme under grant agreement No 821274.

The authors wish to thank Dr. Flaviana Calignano, Associate Professor at Politecnico di Torino, IAM@Polito Interdepartmental Center, for her precious support given during the preparation and development of the manufacturing process.

The authors would like to thank Dr. Manuel Avella Romero for the assistance provided with the TEM characterization

## References

[1] Shirani Bidabadi MH, Yu Z, Rehman A, He JG, Zhang C, Chen H, Yang ZG. High-temperature oxidation behavior of CrMoV, F91 and Mar-M247 superalloys exposed to laboratory air at 550 °C. Oxid Metals 2018;90:401–19. https://doi.org/10.1007/s11085-018-9839-4.

[2] Pröbstle M, Neumeier S, Feldner P, Rettig R, Helmer HE, Singer RF, Göken M. Improved creep strength of nickel-base superalloys by optimized γ/γ′ partitioning behavior of solid solution strengthening elements. Mater Sci Eng 2016;676:411–20. https://doi.org/10.1016/j.msea.2016.08.121.

[3] Kozar RW, Suzuki A, Milligan WW, Schirra JJ, Savage MF, Pollock TM. Strengthening mechanisms in polycrystalline multimodal nickel-base superalloys. Metall Mater Trans A Phys Metall Mater Sci 2009;40:1588–603. https://doi.org/10.1007/s11661-009-9858-5.

[4] Bassini E, Sivo A, Martelli PA, Rajczak E, Marchese G, Calignano F, Biamino S, Ugues D. Effects of the solution and first aging treatment applied to as-built and post-HIP CM247 produced via laser powder bed fusion (LPBF). J Alloys Compd 2022;905:164213. https://doi.org/10.1016/j.jallcom.2022.164213.

[5] Carter LN. Selective laser melting of nickel superalloys for high temperature applications. Sch Metall Mater 2013;298.

[6] Gerstgrasser M, Cloots M, Stirnimann J, Wegener K. Focus shift analysis, to manufacture dense and crack-free SLM-processed CM247LC samples. J Mater Process Technol 2021;289:116948. https://doi.org/10.1016/j.jmatprotec.2020.116948.

[7] Xu J, Brodin H, Peng RL, Luzin V, Moverare J. Effect of heat treatment temperature on the microstructural evolution of CM247LC superalloy by laser powder bed fusion. Mater Char 2022;185:111742. https://doi.org/10.1016/j.matchar.2022.111742.

[8] Langdon TG. Grain boundary sliding revisited: developments in sliding over four decades. J Mater Sci 2006;41:597–609. https://doi.org/10.1007/s10853-006-6476-0.

[9] Langdon TG. Effect of surface configuration on grain boundary sliding. OR Trans 1972;3:797–801. https://doi.org/10.1007/bf02647651.

[10] Gao CY, Zhang LC. A constitutive model for dynamic plasticity of FCC metals. Mater Sci Eng 2010;527:3138–43. https://doi.org/10.1016/j.msea.2010.01.083.

[11] Osetsky YN, Pharr GM, Morris JR. Two modes of screw dislocation glide in fcc single-phase concentrated alloys. Acta Mater 2019;164:741–8. https://doi.org/10.1016/j.actamat.2018.11.020.

[12] Venkataraman A, Linne M, Daly S, Sangid MD. Criteria for the prevalence of grain boundary sliding as a deformation mechanism. Materialia 2019;8:100499. https://doi.org/10.1016/j.mtla.2019.100499.

[13] Masuda H, Sato E. Diffusional and dislocation accommodation mechanisms in superplastic materials. Acta Mater 2020;197:235–52. https://doi.org/10.1016/j.actamat.2020.07.042.

[14] Okada T, Hisazawa H, Iwasaki A, Amimoto S, Miyaji J, Shisawa M, Ueki T. Grain-boundary sliding and its accommodation at triple junctions in aluminum and copper tricrystals. Mater Trans 2019;60:86–92. https://doi.org/10.2320/matertrans.M2018296.

[15] Mikhaylovskaya AV, Yakovtseva OA, Mochugovskiy AG, Cifre J, Golovin IS. Influence of minor Zn additions on grain boundary anelasticity, grain boundary sliding, and superplasticity of Al-Mg-based alloys. J Alloys Compd 2022;926:166785. https://doi.org/10.1016/j.jallcom.2022.166785.

[16] Roodposhti PS, Sarkar A, Murty KL, Brody H, Scattergood R. Grain boundary sliding mechanism during high temperature deformation of AZ31 Magnesium alloy. Mater Sci Eng 2016;669:171–7. https://doi.org/10.1016/j.msea.2016.05.076.

[17] Sandström R, Wu R, Hagström J. Grain boundary sliding in copper and its relation to cavity formation during creep. Mater Sci Eng 2016;651:259–68. https://doi.org/10.1016/j.msea.2015.10.100.

[18] Sabirov I, Estrin Y, Barnett MR, Timokhina I, Hodgson PD. Tensile deformation of an ultrafine-grained aluminium alloy: Micro shear banding and grain boundary sliding. Acta Mater 2008;56:2223–30. https://doi.org/10.1016/j.actamat.2008.01.020.

[19] Tan JC, Tan MJ. Superplasticity and grain boundary sliding characteristics in two stage deformation of Mg-3Al-1Zn alloy sheet. Mater Sci Eng 2003;339:81–9. https://doi.org/10.1016/S0921-5093(02)00097-7.

[20] Koike J, Ohyama R, Kobayashi T, Suzuki M, Maruyama K. Grain-boundary sliding in AZ31 magnesium alloys at room temperature to 523 K. Mater Trans 2003;44:445–51. https://doi.org/10.2320/matertrans.44.445.

[21] Barnett MR, Ghaderi A, Sabirov I, Hutchinson B. Role of grain boundary sliding in the anisotropy of magnesium alloys. Scripta Mater 2009;61:277–80. https://doi.org/10.1016/j.scriptamat.2009.04.001.

[22] Wang YN, Huang JC. Comparison of grain boundary sliding in fine grained Mg and Al alloys during superplastic deformation. Scripta Mater 2003;48:1117–22. https://doi.org/10.1016/S1359-6462(02)00615-2.

[23] Linne MA, Bieler TR, Daly S. The effect of microstructure on the relationship between grain boundary sliding and slip transmission in high purity aluminum. Int J Plast 2020;135:102818. https://doi.org/10.1016/j.ijplas.2020.102818.

[24] Vinogradov A, Hashimoto S, Patlan V, Kitagawa K. Atomic force microscopic study on surface morphology of ultra-fine grained materials after tensile testing. Mater Sci Eng 2001;319–321:862–6. https://doi.org/10.1016/S0921-5093(01)01057-7.

[25] Kottada RS, Chokshi AH. Grain boundary sliding during diffusion and dislocation creep in a Mg-0.7 Pct Al alloy. Metall Mater Trans A Phys Metall Mater Sci 2007;38:1743–9. https://doi.org/10.1007/s11661-007-9190-x.

[26] Torres EA, Caram R, Ramirez AJ. Grain boundary sliding phenomenon and its effect on high temperature ductility of Ni-base alloys. Mater Sci Forum 2010;638–642:2858–63. https://doi.org/10.4028/www.scientific.net/MSF.638-642.2858.

[27] Takizawa Y, Kajita T, Kral P, Masuda T, Watanabe K, Yumoto M, Otagiri Y, Sklenicka V, Horita Z. Superplasticity of Inconel 718 after processing by high-pressure sliding (HPS). Mater Sci Eng 2017;682:603–12. https://doi.org/10.1016/j.msea.2016.11.081.

[28] Morrison RL, Fensin SJ, Carter JLW. Exploration of the sliding behavior of a Σ11 grain boundary with precipitates in Ni–Al system using molecular dynamics. Materialia 2019;7:100383. https://doi.org/10.1016/j.mtla.2019.100383.

[29] Wu ZX, Zhang YW, Jhon MH, Srolovitz DJ. Anatomy of nanomaterial deformation: grain boundary sliding, plasticity and cavitation in nanocrystalline Ni. Acta Mater 2013;61:5807–20. https://doi.org/10.1016/j.actamat.2013.06.026.

[30] Deshpande A. Additive manufacturing of nickel alloys. In: Pei E, Bernard A, Gu D, Klahn C, Monzón M, Petersen M, Sun T, editors. Springer Handb. Addit. Manuf. Cham: Springer International Publishing; 2023. p. 655–69. https://doi.org/10.1007/978-3-031-20752-5_39.

[31] Lam MC, Lim SCV, Song H, Zhu Y, Wu X, Huang A. Scanning strategy induced cracking and anisotropic weakening in grain texture of additively manufactured superalloys. Addit Manuf 2022;52.

[32] Qin H, Fallah V, Dong Q, Brochu M, Daymond MR, Gallerneault M. Solidification pattern, microstructure and texture development in Laser Powder Bed Fusion (LPBF) of Al10SiMg alloy. Mater Char 2018;145:29–38. https://doi.org/10.1016/j.matchar.2018.08.025.

[33] Martelli PA, Sivo A, Calignano F, Bassini E, Biamino S, Ugues D. Parameters optimization and repeatability study on low-weldable nickel-based superalloy rené 80 processed via laser powder–bed fusion (L-PBF). Metals (Basel) 2023;13. https://doi.org/10.3390/met13020210.

[34] Gokcekaya O, Ishimoto T, Hibino S, Yasutomi J, Narushima T, Nakano T. Unique crystallographic texture formation in Inconel 718 by laser powder bed fusion and its effect on mechanical anisotropy. Acta Mater 2021;212. https://doi.org/10.1016/j.actamat.2021.116876.

[35] Zhang X, Xu H, Li Z, Dong A, Du D, Lei L, Zhang G, Wang D, Zhu G, Sun B. Effect of the scanning strategy on microstructure and mechanical anisotropy of Hastelloy X superalloy produced by Laser Powder Bed Fusion. Mater Char 2021;173:1–11. https://doi.org/10.1016/j.matchar.2021.110951.

[36] Mostafaei A, Ghiaasiaan R, Ho I-T, Strayer S, Chang K-C, Shamsaei N, Shao S, Paul S, Yeh A-C, Tin S, To A. Additive Manufacturing of Nickel-based superalloys: a state-of-the-art review on process-structure-defect-property relationship. Prog Mater Sci 2023;136:101108. https://doi.org/10.1016/j.pmatsci.2023.101108.

[37] Lizzi F, Pradeep K, Stanojevic A, Sommadossi S, Poletti MC. Hot deformation behavior of a Ni-based superalloy with suppressed precipitation. Metals (Basel) 2021;11:1–18.

[38] Horikoshi S, Yanagida A, Yanagimoto J. Uniform hot compression of nickel-based superalloy 720Li under isothermal and low friction conditions. Tetsu-To-Hagane/J Iron Steel Inst Japan 2022;108:107–19. https://doi.org/10.2355/tetsutohagane.TETSU-2021-079.

[39] Bassini E, Marchese G, Cattano G, Lombardi M, Biamino S, Ugues D, Vallillo G, Picqué B. Influence of solutioning on microstructure and hardness of hot isostatically pressed Astroloy. J Alloys Compd 2017;723:1082–90. https://doi.org/10.1016/j.jallcom.2017.06.332.

[40] Divya VD, Muñoz-Moreno R, Messé OMDM, Barnard JS, Baker S, Illston T, Stone HJ. Microstructure of selective laser melted CM247LC nickel-based superalloy and its evolution through heat treatment. Mater Char 2016;114:62–74. https://doi.org/10.1016/j.matchar.2016.02.004.

[41] Raj R, Ashby MF. On grain boundary sliding and diffusional creep. Metall Trans 1971;2:1113–27. https://doi.org/10.1007/BF02664244.

[42] Safari J, Nategh S, McLean M. Evolution of microstructure of nickel base superalloy at high temperatures. Mater Sci Technol 2006;22:888–98. https://doi.org/10.1179/174328406X91168.
[43] Chen YQ, Francis E, Robson J, Preuss M, Haigh SJ. Compositional variations for small-scale gamma prime (γ′) precipitates formed at different cooling rates in an advanced Ni-based superalloy. Acta Mater 2015;85:199–206. https://doi.org/10.1016/j.actamat.2014.11.009.
[44] Somekawa H, Singh A, Mukai T, Inoue T. Effect of alloying elements on room temperature tensile ductility in magnesium alloys. Philos Mag 2016;96:2671–85. https://doi.org/10.1080/14786435.2016.1212174.
[45] Du N, Qi Y, Krajewski PE, Bower AF. The effect of solute atoms on aluminum grain boundary sliding at elevated temperature. Metall Mater Trans A Phys Metall Mater Sci 2011;42:651–9. https://doi.org/10.1007/s11661-010-0326-z.
[46] Stinville JC, Yao ER, Callahan PG, Shin J, Wang F, Echlin MP, Pollock TM, Gianola DS. Dislocation dynamics in a nickel-based superalloy via in-situ transmission scanning electron microscopy. Acta Mater 2019;168:152–66. https://doi.org/10.1016/j.actamat.2018.12.061.
[47] Genée J, Signor L, Villechaise P. Slip transfer across grain/twin boundaries in polycrystalline Ni-based superalloys. Mater Sci Eng 2017;701:24–33. https://doi.org/10.1016/j.msea.2017.06.072.
[48] Stinville JC, Vanderesse N, Bridier F, Bocher P, Pollock TM. High resolution mapping of strain localization near twin boundaries in a nickel-based superalloy. Acta Mater 2015;98:29–42. https://doi.org/10.1016/j.actamat.2015.07.016.
[49] Kassner ME. Creep fracture. In: Fundam. Creep Met. Alloy. second ed. Elsevier; 2008. p. 221–46.
[50] Sisanbaev AV, Valiev RZ. The effect of triple junction type on grain-boundary sliding and accomodation in aluminium tricrystals. Acta Metall Mater 1992;40:3349–56. https://doi.org/10.1016/0956-7151(92)90048-J.
[51] Tang YT, Wilkinson AJ, Reed RC. Grain boundary serration in nickel-based superalloy Inconel 600: generation and effects on mechanical behavior. Metall Mater Trans A Phys Metall Mater Sci 2018;49:4324–42. https://doi.org/10.1007/s11661-018-4671-7.